Fusion Engineering and Design 192 (2023) 113777

Contents lists available at ScienceDirect

Fusion Engineering and Design

journal homepage: www.elsevier.com/locate/fusengdes

Scenario trajectory optimization and control on STEP☆

J. Mitchell *, A. Parrott, F.J. Casson, F.E. Eriksson, F. Koechl, M. Lennholm, O. Bardsley, H.F. Meyer, S. Aleiferis

UKAEA-CCFE, Culham Science Centre, Abingdon, OX14 3DB, United Kingdom

ARTICLE INFO

Keywords:
Plasma transport modeling
Optimization
Optimal control problem
Tokamak plasma control
Scenario development
Kinetic control
Ramp-up

ABSTRACT

In this paper we present optimized actuator trajectories, evolving in time and space, of non-inductive ramp-up scenarios for the Spherical Tokamak for Energy Production (STEP). These trajectories are computed by solving a non-linear, multi-objective, constrained, finite-time optimal control problem. A method unique to STEP ramp-up studies that provides an alternative to existing trajectory search strategies which rely on manually adjusting trajectories to reach a desired state. To navigate a non-linear parameter space which is densely populated with local minima, we demonstrate an iterative objective function construction process whereby costs and constraints are included successively and re-optimized after each inclusion to improve convergence and feasibility. This method is particularity useful when the initial trajectory is far from the desired operating space. We use the RApid Plasma Transport simulatOR (RAPTOR) code to self-consistently solve four coupled, 1-D state equations; poloidal flux, electron temperature, ion temperature and electron density. Our STEP actuator trajectories lasting $1500s$, consist of 8 Gaussian electron cyclotron heating and current drive beams distributed across the minor radius, a Deuterium/Tritium particle source and plasma current. We also introduce a modified transport Bohm–gyroBohm model and a new actuator module to RAPTOR which were required to adequately simulate the STEP operating scenarios.

1. Introduction

1.1. Background

The United Kingdom Atomic Energy Authority is currently designing the Spherical Tokamak for Energy Production (STEP) which aims to be the first electricity producing fusion reactor by 2040 [1]. The spherical tokamak (ST) principle enables a more compact machine design, which has the advantage of high β (ratio of plasma pressure to magnetic pressure), β_N (normalized β) and elongation. Hence, ST's produce a higher plasma pressure at lower toroidal field strength, when compared to conventional aspect ratio tokamaks. Typically in a tokamak, inductive current drive using a central solenoid is the primary plasma current actuator, but the limited flux swing of the solenoid restricts these devices to pulsed operation. In ST's, and particularly in STEP, the solenoid flux swing capacity is greatly reduced due to physical space constraints in the central column. The best currently available non-inductive current drive methods for STEP are electron Bernstein wave (EBW) and electron cyclotron heating and current drive (ECHCD). Although these methods are inefficient compared to solenoid driven current and are difficult to control due to strong non-linear couplings with electron temperature and density, they can be used to directly manipulate the current profile, unlike inductively driven current which diffuses restively from the plasma edge.

At present, the proposed STEP ramp-up scenario consists of two stages: the first is outside the scope of this study, but consists of breakdown, burn-through and a short, purely inductive, Ohmic heating phase aimed at getting the plasma current to 2.2 MA, the shape to full bore and the x-points formed. The second phase lasting $\sim$ 1500 s and where our simulation begins, is fully non-inductive and driven by a large ECHCD system. Our ramp-up plasma consists of a 50/50 Deuterium/Tritium mix with an effective ion charge $z_{eff} = 2$ at the core increasing linearly to $z_{eff} = 4$ at the edge, this is to support the high radiative fraction and meet divertor heat load constraints. Radiation losses are taken into account using a profile scaled to 50% of the input power with a fixed shape typical of high radiation fraction experiments. In the absence of validated thermal transport models in our high electron/ion temperature regimes and the lack of experimental data, the purpose of this paper is not to find practically viable solutions, but rather to address the challenges involved in controlling and developing non-inductive ramp-up scenarios.

☆ This material is based upon work supported by the United Kingdom Atomic Energy Authority, Culham Center for Fusion Energy.
* Corresponding author.
E-mail address: joshua.mitchell@ukaea.uk (J. Mitchell).

https://doi.org/10.1016/j.fusengdes.2023.113777
Received 27 October 2022; Received in revised form 4 April 2023; Accepted 20 April 2023
Available online 9 May 2023

1.2. Relation to previous work & motivation

The fully non-inductive ramp-up scenario is particularly challenging. Firstly, the solenoid driven current must be completely replaced by externally driven current sources. Secondly, excessively peaked safety factor profiles (current holes) must be avoided to maintain magnetohydrodynamic (MHD) stability and avoid formation of strong instability driving Internal Transport Barriers (ITBs). Large current holes also cause simulations to become numerically unstable. Thirdly, the current profile must be carefully controlled to avoid excessively large normalized internal plasma inductance, $li(3)$, which leads to an uncontrollable vertical instability and excessively low $li(3)$ which degrades performance. Finally, a balance must be found between non-inductive current drive efficiency, high electron/ion temperatures, input power and a favorable Greenwald Fraction (f_{GW}).

While fully inductive and partially non-inductive ramp-up studies are well researched both numerically and experimentally, there is a considerably smaller body of work covering the optimization of fully non-inductive ramp-up scenarios. Possibly the oldest most directly related source on this topic is [2] in which a simplified analytical approach is taken to realize the optimal input power at which the efficiency of radio-frequency energy converted into poloidal magnetic field energy is maximized and thus the optimal non-inductive current ramp-up rate. This shares similar principles to impedance matching of electrical current sources and loads. Since then, a fully non-inductive ramp-up has only been achieved on a few devices, most recently on QUEST to peak plasma currents > 70 kA in ~ 3 s by injecting 100 kW of EBW at relatively low f_{GW} [3]. The TST-2 spherical tokamak team have also achieved a fully non-inductive ramp-up to one quarter of their typical inductive discharges [4].

Improving on the previous work on NSTX by [5], the simulations conducted by [6] achieved non-inductive ramp-ups at low temperatures with a self-consistent 1.5D transport model (TRANSP) and prescribed time-varying electron density profiles. The lack of feedback control or an optimal trajectory planning scheme in [6] implies that trajectories were found manually through trial and error and the associated difficulties of this strategy are what we aim to mitigate in this paper.

The only other fully non-inductive current ramp-up simulations on similar scales as the scenario in this paper were performed by [7]. Using the JINTRAC-ESCO code for an earlier version of the STEP ramp-up, their simulations focused on scanning the parameter space to ramp plasma current with a zero loop voltage boundary condition at low $f_{GW} \sim 0.25$. Although successful, the current drive profiles, input f_{GW} and heating required manual tailoring to avoid strong shear reversal, current holes or sudden loss of current. Building on this work we have updated and implemented the RApid Plasma Transport simulatOR (RAPTOR) and its optimization framework to speed up the process of finding non-inductive ramp-up trajectories. RAPTOR is a reduced physics model intended for rapid profile evolution in which four 1-D state equations are self-consistently evolved; poloidal flux, electron and ion temperature and electron density [8]. Unlike in previous works, our simulations use 10 actuators (plasma current, 8 x ECHCD beams, 1 x particle source) to manipulate the trajectories toward a non-inductive state using optimal control techniques.

1.3. Paper outline

This paper is organized as follows:

- Section 2: a brief formulation of the MHD transport physics used in this study,
- Section 3: covers the optimization method used,
- Section 4: details the formulation of the optimal control problem,
- Section 5: results are provided and discussed,
- Section 6: conclusions are given.

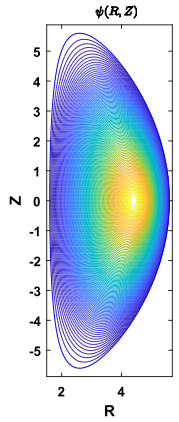

STEP PLASMA FLAT-TOP PERFORMANCE	
Fusion Power (MW)	1760
Net Electric Power (MW)	154
Fusion Gain Q	11.7
Plasma Current (MA)	20
Toroidal Mag. Field (T)	3.2
Confinement Factor, $H_{98(y,2)}$	1.1
Normalised Beta, β_N (%)	4.4
Greenwald Fraction	1.0
Radiation Fraction	0.7
Bootstrap Fraction	0.81
Plasma Major Radius (m)	3.6
Elongation (x-point)	2.8
Aspect ratio	1.8

Fig. 1. A JINTRAC generated equilibrium of the SPR45 STEP design concept recomputed by CHEASE [10]. This equilibrium is shown without divertor legs or x-points, however this is only a limitation of the equilibrium generation in JINTRAC and does not significantly affect the core plasma physics. The size of this equilibrium is set by the inboard build and the ST requirement on aspect ratio $A \leq 2.0$. The center column is constrained to a minimum of 1.6 m to allow space for necessary components. The elongation is the maximum that can be realistically controlled. Triangularity is set to the maximum that the poloidal field coils can support since pedestal performance is proportional to triangularity squared according to ideal MHD peeling-ballooning theory.

2. Tokamak plasma transport: MHD

2.1. Magnetic equilibrium geometry

Although iteratively coupled or externally prescribed time-varying geometry is within RAPTOR's capability [9], all simulations in this study were done with fixed equilibrium geometry. Our simulations start from a full bore plasma at the end of the inductive phase, where we intend no further changes to the plasma shape. The particular equilibrium under study is referred to as SPR45 and is shown in Fig. 1. It is a highly elongated plasma and thus has strict $li(3)$ constraints to maintain vertical controllability. The free-boundary Grad–Shafranov equilibrium solver ESCO, embedded in JINTRAC, was used to generate an initial set of equilibria which where then ported into the CHEASE-RAPTOR format.[1]

2.2. Poloidal flux diffusion

Eq. (1) defines the parabolic partial differential equation (PDE) used in RAPTOR to describe the distributed poloidal magnetic flux $\psi(\rho, t)$ evolution in time and 1D space with Neumann boundary conditions (2) and (3), [11]. Where $V'_\rho = \frac{\partial V}{\partial \rho}$ is the volume gradient, $F = RB_\phi$ is the normalized poloidal current function and g_2, g_3 are flux surface geometric terms calculated using CHEASE. The toroidal flux contained by a given flux surface, $\rho = \sqrt{\Phi/\pi B_0}$, is used as the spatial variable, Φ is the toroidal magnetic flux enclosed by a poloidal flux surface, B_0 is the toroidal magnetic field on axis and $G_2 = \frac{F}{B_0 16\pi^4}\frac{g_2 g_3}{\rho}$. We assume the time derivative $\dot{B}_0 = 0$. For more details see [11].

$$\sigma_\parallel \left(\frac{\partial \psi}{\partial t}\bigg|_\rho - \frac{\rho \dot{B}_0}{2B_0}\frac{\partial \psi}{\partial \rho} \right) = \frac{F^2}{16\pi^4 \mu_0 B_0^2 \rho}\frac{\partial}{\partial \rho}\left[\frac{g_2 g_3}{\rho}\frac{\partial \psi}{\partial \rho}\right] - \frac{V'_\rho}{2\pi\rho}(j_{bs} + j_{ec}), \tag{1}$$

$$\frac{\partial \psi}{\partial \rho}\bigg|_{\rho=0} = 0, \tag{2}$$

$$\left[\frac{G_2}{\mu_0}\frac{\partial \psi}{\partial \rho}\right]_{\rho=\rho_e} = I_p(t). \tag{3}$$

[1] RAPTOR has COCOS = 11, with $\sigma_{I_p} = \sigma_{\beta_\phi} = 1$, following the COCOS coordinate convention [10].

The neoclassical electrical conductivity, $\sigma_{\parallel}$ and the bootstrap current, $j_{bs} = \frac{\langle \mathbf{j}_{bs} \cdot B \rangle}{B_0}$, are defined by the well known Sauter models [12]. The auxiliary driven non-inductive current source provided by the ECHCD system, $j_{ec} = \frac{\langle \mathbf{j}_{ec} \cdot B \rangle}{B_0}$, is defined heuristically, see 2.5.

2.3. Thermal transport

Eq. (4) defines the PDE for the evolution of thermal transport in time and 1D space for species s, with Dirichlet conditions given at the plasma boundary [13].

$$\frac{3}{2}(V'_\rho)^{-5/3}\left(\frac{\partial}{\partial t}\bigg|_\rho - \frac{\dot{B}_0}{2B_0}\frac{\partial}{\partial \rho}\rho\right)[(V'_\rho)^{5/3} n_s T_s] + \frac{1}{V'_\rho}\frac{\partial}{\partial \rho}\left(-\frac{g_1}{V'_\rho} n_s \chi_s \frac{\partial T_s}{\partial \rho} + \frac{5}{2} T_s \Gamma_s g_0\right) = P_s, \tag{4}$$

$$\Gamma_s = -\frac{g_1}{V'^2_\rho} D_s \frac{\partial n_s}{\partial \rho} + \frac{g_0}{V'_\rho} V_s n_s. \tag{5}$$

where $T_s(\rho, t)$, $n_s(\rho, t)$, $\chi_s(\rho, t)$ and $\Gamma_s(\rho, t)$ are the temperatures, densities, thermal diffusivity and convective fluxes of the considered species. P_s is the sum of power density sources and sinks and g_0, g_1 are magnetic equilibrium geometry terms. For more details on these see [8].

2.4. Particle transport

Eq. (6) defines the PDE for the evolution of particle transport in time for electrons. Where D_s is the particle diffusion, and V_s the positive outward particle pinch. Similarly to the thermal transport equation, Dirichlet conditions are given at the plasma boundary [13]. Ion particle transport was arbitrarily scaled to $n_i = 0.9 n_e$.

$$\frac{1}{V'_\rho}\left(\frac{\partial}{\partial t}\bigg|_\rho - \frac{\dot{B}_0}{2B_0}\frac{\partial}{\partial \rho}\rho\right)[(V'_\rho) n_e] + \frac{1}{V'_\rho}\frac{\partial}{\partial \rho}\left(-\frac{g_1}{V'_\rho} D_s \frac{\partial n_s}{\partial \rho} + g_0 V_s n_e\right) = S_e \tag{6}$$

2.5. Sources & sinks

The ECHCD module is implemented according to [8], but worth reviewing here due to its importance in this study. This actuator model has two components, a heating source, $p_{ec}(\rho, t), [\mathrm{W/m^3}]$, defined in Eq. (7) and an electron cyclotron current drive (ECCD) source, $j_{ec}(\rho, t), [\mathrm{A/m^2}]$, defined in Eq. (8). Our ECHCD system consists of 8 Gaussian actuators with fixed widths of $\omega_{dep,e} = 0.25$, equally spaced across ρ from 0 to 0.8 and a peak current drive efficiency of the order 160 kA/MW in the low f_{GW} regime.

$$p_{ec}(\rho, t) = P_{ec}(t) \exp\left\{\frac{-4(\rho - \rho_{dep,e})^2}{\omega^2_{dep,e}}\right\} \Big/ \int_0^{\rho_e} \exp\left\{\frac{-4(\rho - \rho_{dep,e})^2}{\omega^2_{dep,e}}\right\} V' d\rho, \tag{7}$$

$$j_{ec}(\rho, t) = \varepsilon_{cd} e^{-cd_{trap}\rho^2/0.25} \frac{T_e}{n_e} p_{ec}(\rho, t). \tag{8}$$

The total ECCD source efficiency in Eq. (8), is dependent on T_e, n_e, the current drive efficiency scalar $\varepsilon_{cd}(\rho)$ and the trapped particle fraction, cd_{trap} which we set to zero to simplify the problem. To further simplify the problem we chose a flat $\varepsilon_{cd}(\rho)$ profile with a conservative magnitude of $3.78e15, [\mathrm{A\ m^{-2}\ W^{-1}\ eV^{-1}}]$. The GRAY code, [14], was used by [15] to estimate an upper limit on the global dimensionless ECCD efficiency factor ξ_{cd}, defined by [16] and shown in Fig. 2. For our simplified local $\xi_{cd}(\rho)$ model, we assume that the global dimensionless ECCD efficiency is locally valid such that:

$$I_{ec} = \int \frac{V'_\rho}{2\pi F} \langle \mathbf{j}_{ec} \cdot B \rangle d\rho, \tag{9}$$

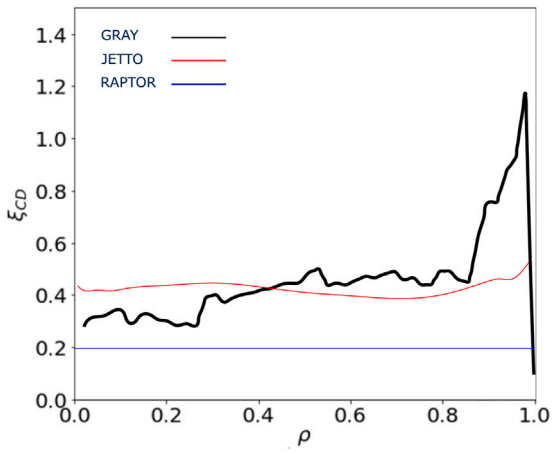

Fig. 2. An estimate upper limit of the global dimensionless ECCD efficiency ξ_{cd} [16], calculated by [15] using the GRAY code [14] for SPR45. This is compared to the local $\xi_{cd}(\rho)$, see Eq. (16), used in these RAPTOR simulations and JINTRAC non-inductive ramp-up studies by [7].

$$dI_{ec} = \frac{V'_\rho B_0}{2\pi F} j_{ec} d\rho, \tag{10}$$

$$P_{ec} = \int V'_\rho p_{ec} d\rho, \tag{11}$$

$$dP_{ec} = V'_\rho p_{ec} d\rho, \tag{12}$$

$$\xi_{cd}(\rho) = 3.27 R_0[\mathrm{m}] \frac{dI_{ec}[A]}{dP_{ec}[\mathrm{W}]} \frac{n_e[10^{-19}\ \mathrm{m^{-3}}]}{T_e[\mathrm{KeV}]}. \tag{13}$$

Where $B_0[T]$ is the toroidal magnetic field on axis and R_0 is the major radius. After substituting Eqs. (10) and (12) into Eq. (13) and re-scaling n_e to $[\mathrm{m^{-3}}]$ and T_e to [eV]:

$$\xi_{cd}(\rho) = \frac{3.27 R_0[\mathrm{m}] B_0[T]}{2\pi F[\mathrm{m\ T}]} \frac{j_{ec}[\mathrm{A\ m^{-2}}]}{p_{ec}[\mathrm{W\ m^{-3}}]} \frac{n_e[\mathrm{m^{-3}}]}{T_e[\mathrm{eV}]} \frac{10^3}{10^{19}} \tag{14}$$

We then rearrange Eq. (8) without the trapped particle fraction term, to arrive at:

$$\varepsilon_{cd}(\rho) = \frac{j_{ec}[\mathrm{A\ m^{-2}}]}{p_{ec}[\mathrm{W\ m^{-3}}]} \frac{n_e[\mathrm{m^{-3}}]}{T_e[\mathrm{eV}]} \tag{15}$$

Making the appropriate substitutions of Eq. (15) into Eq. (14) we arrive at a local form factor for $\xi_{cd}(\rho)$:

$$\xi_{cd}(\rho) = 3.27 R_0 \frac{B_0}{2\pi F} \varepsilon_{cd}(\rho) 10^{-16} \tag{16}$$

Using Eq. (16) we show in Fig. 2 that our chosen $\varepsilon_{cd}(\rho)$ is conservative.

Alpha power, electron–ion equipartition power, Ohmic power and Bremsstrahlung models are self-consistently calculated for simulations detailed in this paper. Line-radiation is included as a scaled input, $P_{rad} = 0.5 P_{ec}$, with an estimated profile of what we aim to achieve on STEP during this phase through adequate impurity control, see Fig. 6.m. The ideal scenario is one where radiation in the core is minimized to help maintain the core temperatures and hence maximize fusion power for given input heating. A peak in radiation just before the LCFS is desired to help minimize the charged particle power that reaches the scrape-off layer, since almost all this power will be lost to the divertors. We assume the presence of lower Z_{eff} impurities in the plasma core with impurity seeding at the edge being used as part of a control system to limit the heat flux on plasma facing components. Impurity seeding to reduce the heat flux to plasma facing component is a method relevant for many fusion pilot plants [17] and the use of impurities for heat flux control has been demonstrated on ASDEX Upgrade [18]. The shape of the P_{rad} profile that may be achievable is

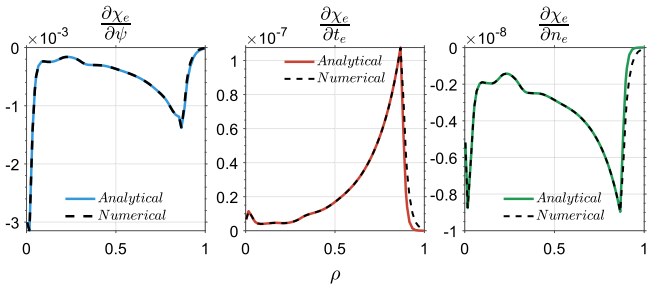

Fig. 3. In this figure we compare the BgB model's analytical and numerical Jacobians w.r.t each state variable (excluding ions) for one time-slice in the discharge. The numerical parts were calculated by running the BgB model once and then again in three separate instances where the input states $\partial\psi, \partial T_e$ and ∂n_e are slightly perturbed. We then take the difference between the original and perturbed BgB output. There is good agreement between both methods, but there is some discrepancy in the regions for $\rho > 0.9$ for ∂T_e and ∂n_e. Future work will aim to mitigate this minor issue.

dependent on the transport of the impurities in the core. The use of codes such as TRANSP for estimating the diffusion of impurities has been used in ASDEX Upgrade core radiation analyses [19] as well as in modeling of the radiation profiles expected in SPARC [20]. The analysis conducted for SPARC similarly started with a spatially uniform value of $Z_{eff} = 1.5$ as an input to their simulations, however their resulting analysis concluded an increasing radiation profile from the center to the edge of the LCFS [20]. The uncertainty associated with the P_{rad} profile scaling and shape used in this study has not been quantified for STEP and remains part of future work; the purpose of this work is to explore a general method.

The electron density particle equation was modified to include a continuous-pellet actuator modeled as a simple normalized Gaussian:

$$s_{ne}(\rho,t) = S_{ne}(t)\exp\left\{\frac{-4(\rho-\rho_{dep,e})^2}{\omega^2_{dep,e}}\right\} \Big/ \int_0^{\rho_e} \exp\left\{\frac{-4(\rho-\rho_{dep,e})^2}{\omega^2_{dep,e}}\right\} V' d\rho \tag{17}$$

This is an important feature, as will be shown later, because the ramp-up is highly sensitive to density evolution.

2.6. Extensions to particle and energy transport models

RAPTOR has a variety of transport models available to simulate thermal and particle diffusion at low magnetic shear [11]. The empirical mixed Bohm–gyroBohm (BgB) model [21] used in this study was modified in order to achieve the high performance operating scenarios demonstrated in JINTRAC runs [7]. Plasma transport is dominated by turbulence and the fusion performance by the H-mode pedestal. Both phenomena are not well understood particularly in ST regimes and our current models feature large uncertainties. Gyro-kinetic codes provide a better picture, but with high computational cost they are not suitable for long-time scale simulations or rapid scenario development. From this perspective, simplified (semi-empirical) models are justified to gain computational performance at the cost of accuracy, while we await the development of improved reduced-models for STEP. Our operating scenarios feature electron temperatures in excess of 40 keV, high and low f_{GW}, and high β_N. Since, no experimental data exists for these regimes with ST geometry, we use semi-empirical transport models calibrated on existing machines and scalings which have been verified using JINTRAC. What is important is not the accuracy of our model, but the optimization method which can theoretically be applied to any transport model which has analytically computable Jacobians.

H-mode and pedestals. The first modification to the BgB model was a simple transport pedestal feature, whereby a fixed pedestal is imposed through the multiplication of a suppression factor toward the outer edges of the $\chi_s(\rho)$ profiles. The pedestal suppression factor is an exponential function prescribed by decay rate (ρ^*_∇), width (ρ^*_{ped}) and minimum edge value ($\chi_{s,min}$), Eq. (18). In order to simplify the calculation of the analytical Jacobians $\frac{\partial \chi_s}{\partial x}$, a mapping is found between the fitted pedestal, Eq. (19), and the original BgB profile so that a new "continuous" profile Eq. (20) can be calculated. This process is done every time-step which allows the pedestal height to vary with the BgB transport model and $H_{98(y,2)}$ confinement feedback scaling as detailed by Eq. (24). The pedestal width can be fixed or time varying, but for this study it was fixed to 12% of ρ. This value was chosen for numerical stability and because the overall pedestal shape compared well with JINTRAC simulations.

$$f_{ped} = (\chi_s(\rho^*_{ped}) - \chi_{s,min}) e^{\rho^*_\nabla(\rho - \frac{\rho^*_{ped}}{\rho})} + \chi_{s,min}, \tag{18}$$

$$\chi_{e,fitted}(\rho) = \begin{cases} \chi_s, & \text{if } \rho \le \rho^*_{ped} \\ f_{ped}, & \text{otherwise} \end{cases}, \tag{19}$$

$$M_s = \chi_{e,fitted} \oslash \chi_s, \tag{20}$$

$$\chi_{s,PED} = M_s \chi_s. \tag{21}$$

where the $\oslash$ operator is element-wise division.

$H_{98(y,2)}$ Confinement feedback. The second modification was the inclusion of a closed loop confinement factor controller which scales the BgB coefficients, forcing a target confinement through feedback, in this case the confinement target is based on the international scaling $H_{98(y,2)} = 1.1$. Although $H_{98(y,2)}$ scaling may not accurately predict ST performance, it is based on a large data set that includes spherical tokamaks [22]. Other ST scalings such as in [23] are more favorable for STs and would predict a much higher confinement than $H_{98(y,2)}$ for STEP, however they are based on sparse datasets that cover a small number of machines and also have significant uncertainty when scaling to a device like STEP. Therefore, $H_{98(y,2)}$ scaling is used as a more conservative choice with a slightly raised target of 1.1. Similar techniques have been implemented in JINTRAC [7] and in [9], however our proportional integral (PI) based controller is bounded by an inverse exponential function Eq. (23). This prevents a negative control output when the error is positive, allowing operation over the whole range of positive and negative error. To avoid numerical issues, the pedestal is assigned first as in Eq. (21) and then the feedback scaling as in Eq. (24). Note that the same fb_{out} is applied to both electron and ion sources.

$$E(t) = H_{98(y,2)}(t) - H_{98(y,2),ref}(t), \tag{22}$$

$$fb_{out}(t) = (e^{-(K_p E(t) + \int K_i E(t) dt)})^{-1}, \tag{23}$$

$$\chi_{s,scaled}(\rho,t) = fb_{out}(t)(\chi_{s,fped}(\rho,t)). \tag{24}$$

This pedestal and $H_{98(y,2)}$ scaling also affects the particle transport because the electron diffusivity and pinch velocity are calculated using the '$\chi_e - scaling$' model. Essentially D_s and V_s from Eq. (6), are set linearly proportional to $\chi_{e,scaled}(\rho,t)$, such that $D_s(\rho,t) = \alpha_D \chi_{e,scaled}(\rho,t)$ and $V_s(\rho,t) = \alpha_V D_s(\rho,t)$, where α_D, α_V are prescribed fixed or time varying scalars.

Analytical Jacobians of the modified Bohm–gyroBohm model. The inclusion of electron density Jacobian Eq. (25) was implemented to give a more up to date Jacobian w.r.t all states, Eq. (26). Where $\alpha_{B,s}$ is the Bohm scaling term per species. In Eq. (27) the confinement feedback scaling and pedestal were then included, where s refers to species. A comparison between the analytical and numerical Jacobians is shown in Fig. 3.

$$\frac{\partial \chi_s}{\partial n_e} = \alpha_{B,s} \frac{-2|\nabla ne|.q^2.T_e}{B_t.n_e^2}, \tag{25}$$

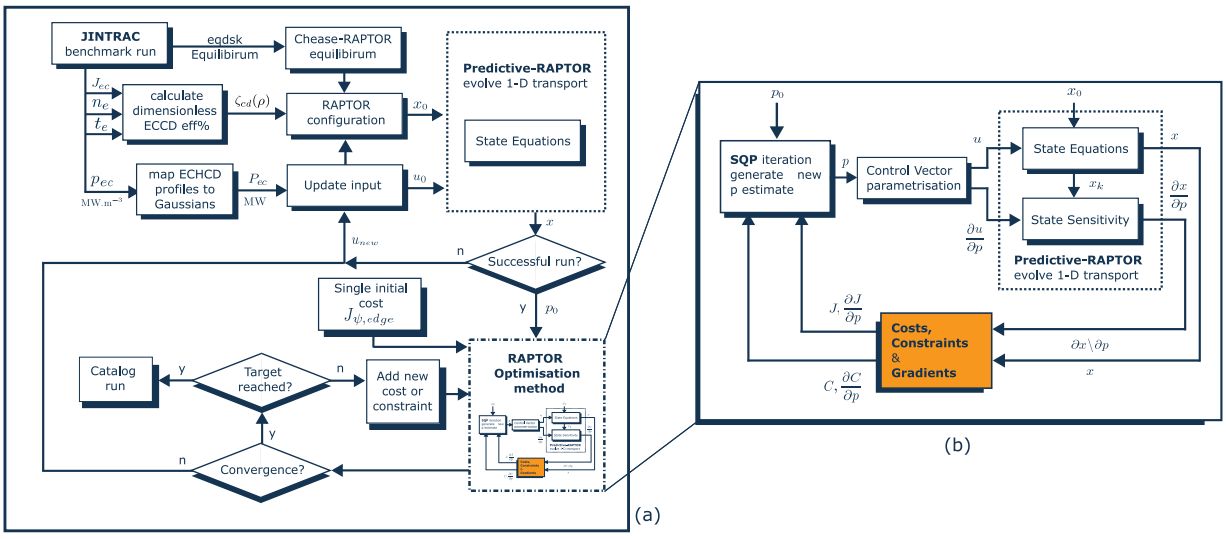

Fig. 4. A simplified diagram of the optimization processes used in this study. (a) illustrates how initial JINTRAC trajectories are provided and refined. Costs and constraints are then added until targets are met while keeping the number of time knots fixed. (b) a closer look at the RAPTOR Sequential Quadratic Programming process, where states are evolved using the selected control vector p_0, after which state sensitivities are calculated to facilitate further calculation of the cost and constraint Jacobians.

$$\frac{\partial \chi_s}{\partial x} = \frac{\partial \chi_s}{\partial n_e}\frac{\partial n_e}{\partial x} + \frac{\partial \chi_s}{\partial T_e}\frac{\partial T_e}{\partial x} + \frac{\partial \chi_s}{\partial \psi}\frac{\partial \psi}{\partial x}, \tag{26}$$

$$\frac{\partial \chi_{s,scaled}}{\partial x} = f b_{out}(t) M_s \frac{\partial \chi_s}{\partial x}. \tag{27}$$

3. Optimization method

The Sequential Quadratic Programming (SQP) algorithm [24], from the MATLAB Optimization Toolbox, was predominantly used to solve the optimization problems in this study and the interior-point algorithm was used to cross check convergence and solutions. Both algorithms require local estimates of objective functions and their gradients. Long timescale discharges (> 1000 s) make it computationally intractable to compute gradients using finite difference methods. Predictive-RAPTOR overcomes this by simplifying the formulation of objective functions and their gradients using state sensitivities as formulated in Section 4.

Both algorithms are local minimum solvers, thus it is important to provide a reference trajectory that is as close as possible to the local minimum desired, and if possible with all constraints satisfied. Anything sufficiently far away from the desired minimum was found to end in poor feasibility or badly satisfied constraints. To reduce the tedious process of manually adjusting trajectories to reach the operating point, an iterative process was developed to gradually build the objective functions, starting with a simple cost function with few or no constraints. This process is illustrated in Fig. 4. The very first references, taken from JINTRAC runs in [7], were modified slightly to make the simulations numerically stable in RAPTOR. A single input single output PI based f_{GW} feedback controller acting only on S_{ne} was used to plan the starting f_{GW} trajectory and then removed for the optimization process so that the control vector acts directly on S_{ne}.

4. Formulation of the optimal control problem

In this section we briefly formulate the non-linear, constrained optimization problem. We make several changes to the optimization problem posed in [8,9]. Firstly, all the cost functions and constraints in this study are active for the entire discharge and not just the end time point, secondly, we add several new constraints and finally, we use 8 ECHCD actuators and a new particle source actuator. Our time step and time horizon are also significantly larger, 2 s and 1500 s respectively. The time step is large to cope with the computational burden of the significantly longer 1500 s discharge periods. With this step size a single discharge takes approximately 2 and 5 minutes, depending on numerical convergence for each time-step. For 1 optimization run the process can take up to 8 hours, depending on optimization feasibility and the number of degrees of freedom (time-knots).

4.1. Control vector parametrization

In order to reduce the degrees of freedom in the optimization problem, the prediction horizon can be discretized into manageable piece-wise chunks by parametrizing the continuous actuator input vector in time. The ith actuator input vector $u_i(t)$ is discretized as a set of parameters $p \in \Re^{n_p}$ written as:

$$u_i(t) = \sum_j^{n_i} P_{ij}(t) p_{i,j} \tag{28}$$

$P_{ij}(t)$ is a scalar piece-wise linear or piece-wise constant function (with finite support), $p_{i,j}$ is a weighting scalar and n_i is the number of parameters which defines the ith actuator trajectory [8].

Upper and lower boundaries on the actuators are cast into linear inequality constraints described by Eq. (29). They are formulated directly on elements of the parameter vector p and are illustrated in Fig. 5.

$$A_{ineq} p \leq b_{ineq} \tag{29}$$

4.2. Cost function definition

The cost function to be minimized is defined in Eq. (30) as the sum of weighted 2 norm time integrals. The integrals are arranged in descending order of importance with the minimization of the flux swing at the top. The individual analytical cost function gradients w.r.t the control vector p in Eq. (31) are calculated using chain rule and the state sensitivity, $\frac{\partial x}{\partial p}$, where x is the system state vector and $\frac{\partial u}{\partial p}$ the actuator sensitivity, where u is the actuator input vector and J_i is a generic cost function formulated as shown in Eq. (30).

$$J = \overbrace{\int_{t_0}^{t_f} \|\psi_{edge}\|^2_{W_1} dt}^{\min(\psi_{edge})\forall t} + \overbrace{\int_{t_0}^{t_f} \|li(3) - 0.3\|^2_{W_2} dt}^{\min(li(3)-0.3)\forall t}, \tag{30}$$

$$\frac{dJ_i(x,u)}{dp} = \frac{\partial J_i}{\partial x}\frac{\partial x}{\partial p} + \frac{\partial J_i}{\partial u}\frac{\partial u}{\partial p}. \tag{31}$$

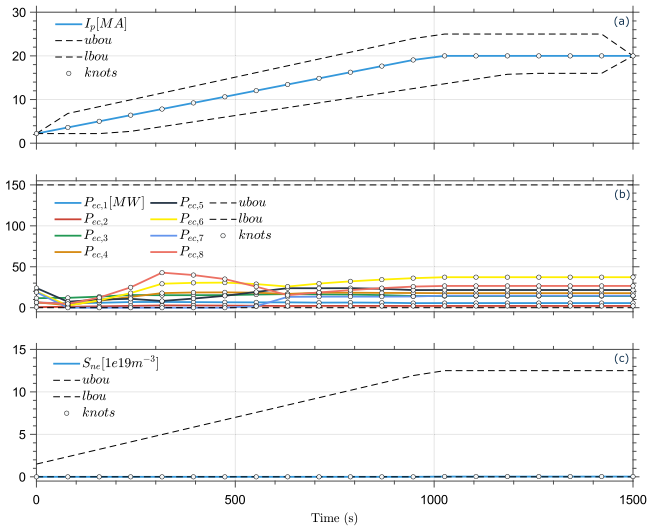

Fig. 5. Plots (a) to (b) illustrate the upper and lower boundary constraints on the 10 actuators with the upper bounds (ubou), lower bounds (lbou) and the parametrized control vector time knots. In (a) the plasma current is upper bounded by 125% and lower bounded by 80% off the nominal trajectory. Note that the initial and final points are fixed to 2.2MA and 20MA respectively. In (b) the input auxiliary power is lower bounded to zero and each actuator has a large upper bound of 150 MW. Finally in (c) the particle source is upper bounded to $12.5e19$ m^{-3} and lower bounded to 0.

4.3. State trajectory constraints

The following state constraints have been chosen, starting with Eq. (32), a hybrid scenario lower limit on the safety factor which takes advantage of improved confinement and avoids sawtooth crashes and other MHD instabilities or disruptions. Eq. (33) prevents disruptions due to the Greenwald fraction limit, where the fraction of this limit is computed as $f_{GW} = \langle n_e \rangle_V \frac{I_p[MA]}{2\pi a}$, where a is the minor radius and $\langle n_e \rangle_V = \frac{\int n_e[10^{-20}\ \mathrm{m}^{-3}]dV}{V}$ is the volume averaged plasma density. Eq. (35) is to avoid run-away electrons. Eq. (36) prevents β_N disruptions. Eq. (37) avoids high $li(3)$ which leads to vertical instability and Eq. (38) avoids low $li(3)$, to allow divertor shaping and maintain good confinement.

$$C_{q \geq l_{lim}}(\rho, t) \geq 2 \,\forall t, \tag{32}$$

$$C_{f_{GW} \leq u_{lim}}(t) \leq 1 \,\forall t, \tag{33}$$

$$C_{f_{GW} \geq l_{lim}}(t) \geq 0.2 \,\forall t, \tag{34}$$

$$C_{T_e \leq u_{lim}}(t) \leq 70 \text{ KeV } \forall t, \tag{35}$$

$$C_{\beta_N \leq u_{lim}}(t) \leq 4.4 \,\forall t, \tag{36}$$

$$C_{li(3) \leq u_{lim}}(t) \leq 0.4 \,\forall t, \tag{37}$$

$$C_{li(3) \geq l_{lim}}(t) \geq 0.25 \,\forall t. \tag{38}$$

The constraints are formulated as in [8] and denoted $C_i(t, x(t)) \leq 0$ for the ith constraint. Constraints dependent on ρ are checked for limit violations along ρ and then integrated first over ρ Eq. (39), convexified and then integrated over the desired time period, in this case Eq. (40) is $\forall\ t$. Note that ε is a relaxation parameter to ensure $\frac{\partial C_i}{\partial x} \neq 0$ when $C_i(\rho) = 0$ [6].

$$c_i(t) = \int_0^{\rho_e} \max\left[0, (i(\rho, t) - i_{lim})\right] d\rho, \tag{39}$$

$$C_{i \leq i_{lim}} = \int_{t_0}^{t_f} c_i(t)^2 dt - \varepsilon \leq 0, \tag{40}$$

The constraint gradients in Eq. (41) are tackled in a similar fashion to the cost functions.

$$\frac{dC_{i \leq i_{lim}}}{dp} = \int_{t_0}^{t_f} 2 \max\left[0, c_i(t, x)\right] \frac{\partial c_i(t, x)}{\partial x} \frac{\partial x}{\partial p} dt. \tag{41}$$

The final optimal problem can be written as:

$$\min J = J(x(t), u(t)) \tag{42}$$

such that

$$f(x(t), u(t), t) = 0 \,\forall t \tag{43}$$

$$u_i(t) = \sum_j^{n_i} P_{ij}(t) p_{i,j} \tag{44}$$

$$A_{ineq} p \leq b_{ineq} \tag{45}$$

$$C(x(t)) \leq 0 \tag{46}$$

5. Results & discussion

The evolution of the last optimized trajectories for the 1500s ramp-up scenario are illustrated in Fig. 6.a-j. The first of these was optimized with only $J_{\psi,edge}$ and constraint Eqs. (33), (34) and (36). This result was then passed through the optimizer again, but with a modified objective function. The second trajectory was optimized with only $J_{\psi,edge}$, J_{li3} and Eqs. (32)–(36). Only the final trajectory, illustrated by solid-lines, was optimized with the full set of costs and constraints given in Section 4, using the interior-point algorithm. We want to emphasize that if the first reference trajectory is optimized with the full objective function, the solver does not converge, since over-constraining the parameter space while the trajectory lies outside the constrained region, prevents the solver from adequately navigating to a local minima. This issue occurs frequently if ψ_{edge} is constrained too early on and in this particular run we avoided constraining it entirely. In Fig. 6.e the peak ψ_{edge} and $\Delta\psi_{edge}$ have been reduced from first trajectory by an order of magnitude. In the second trajectory $\Delta\psi_{edge}$ is within 400 mWb, but due to the addition of the $li(3)$ constraint in the final trajectory, $\Delta\psi_{edge}$ rises to 800 mWb. The large starting ECHCD power of $\sim$ 100 MW in Fig. 6.b, mitigates the initial spike in ψ_{edge}. This was one of the most prominent features that almost all optimizations runs in this study found. Due to this heavy initial power load on the divertor heat flux ($\sim$ 50 MW), the starting edge density is set to $1.5e19$ m^{-3} and increases linearly (prescribed as a boundary condition) to $3e19$ m^{-3} at 1000 s after which it remains at this value. In the current design, the solenoid constraint is so strict that to prevent quenching, absolutely no current can be present in the coil during ramp-up, this may not be the case in this run, but the argument could be made that the remaining flux swing can be compensated by poloidal field coil contributions alone. In any case, for RAPTOR to simulate absolutely zero ψ_{edge}, the boundary condition in Eq. (3) will need to be changed to either a Dirichlet or a Robin boundary condition. This has not yet been implemented, but will be in future work. At 1500 s the desired flat-top current has been reached. The process of reaching steady-state and increasing the density to burning plasma conditions, will be part of the flat-top trajectory optimization, which is outside the scope of this paper.

In Fig. 6.f we see that the reference f_{GW} trajectory decays to the lowest possible value to maximize the current drive efficiency. However, before 100 s the optimizer chooses a counter-intuitive path that initially increases the f_{GW} using a combination of S_{ne} in Fig. 6.c, I_p in Fig. 6.a & P_{ec} in Fig. 6.b for the first 100 s. This has the combined affect of reducing $li(3)$ in Fig. 6.c and maintaining a steady T_e rise in Fig. 6.g, which prevents the plasma from becoming too conductive early on. It also increases the controllability of the q-profile in the discharge and reduces the plasma back-EMF. Although the increased density helps to distribute the plasma current and bring down $li(3)$, the optimizer does not reach the $li(3) = 0.3$ target perfectly. The reason for this is that the two active cost functions are conflicting in descent directions for most of the discharge as shown in Fig. 7. It is an optimization problem in itself to find perfectly balanced weighting factors, and in other simulation trials where the relative cost weight of $l_i(3)$ was increased, it resulted in larger perturbations in ψ_{edge} violating

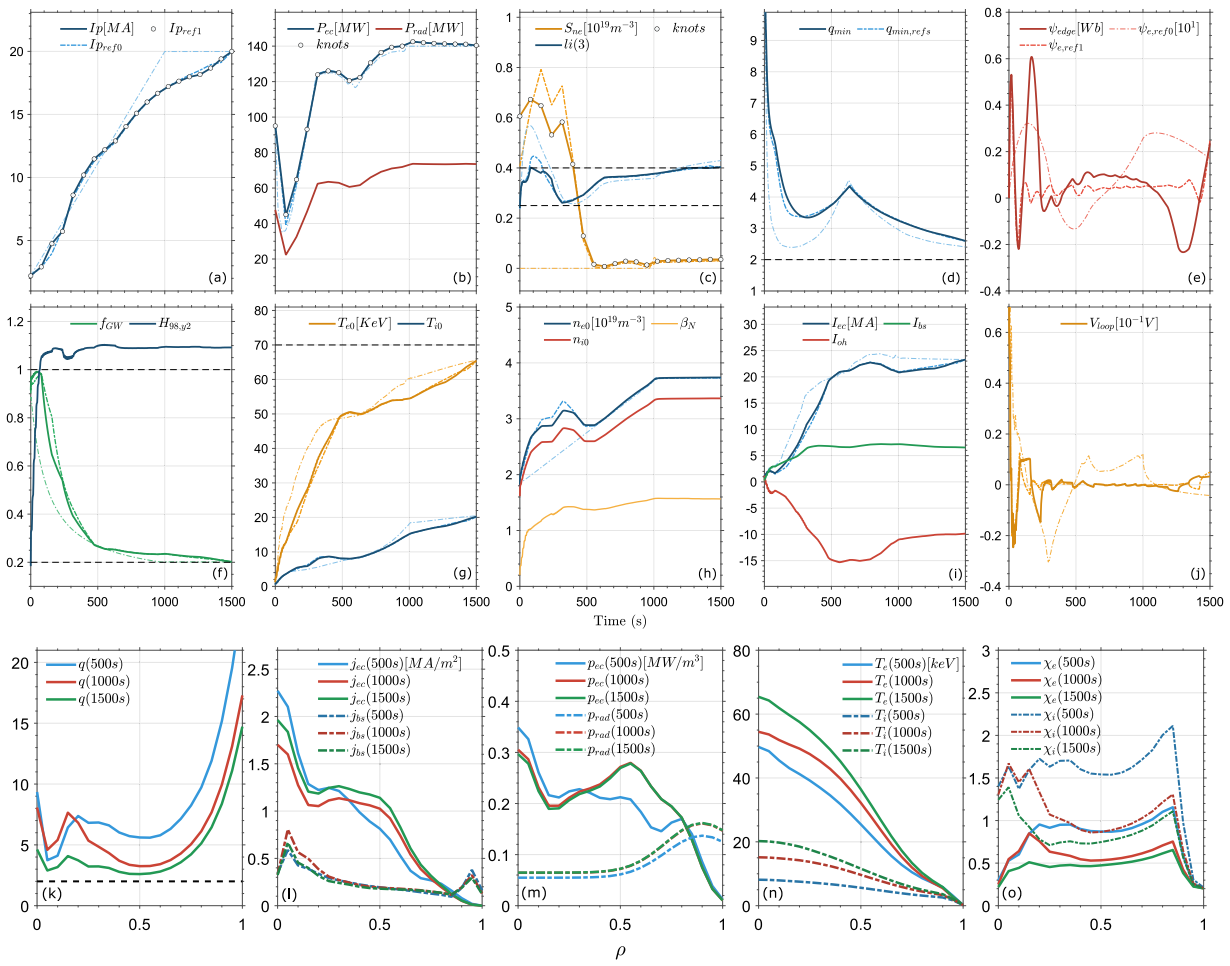

Fig. 6. Subplots (a) to (j) illustrate the actuator inputs, plasma quantities and states evolved over the 1500 s discharge. In every figure there are solid and dash–dot-lines. The solid lines represent the final optimized trajectory that satisfies all constraints. The dash–dot-lines represent the last two optimized reference trajectories, indicated in (a) as $I_{p,0}$ and $I_{p,1}$ and are shown in increasing thickness in the same color as the final optimized solid-line signals. The black dashed-lines indicate constraints. On the actuator signals there are "o" markers which indicate the parametrized control vector time knots that are linked together piece-wise linearly to form the "continuous" solid lines, see Eq. (28). Subplots (k) to (o) illustrate the final optimized trajectory profiles across the minor radius for three time points in the discharge 500 s, 1000 s, 1500 s. Note: Assume equal scaling and units for all signals in the plot, if signal scaling or units are not explicitly indicated.

the requirements. It is the active constraint on $li(3)$ that is responsible for forcing the value to ≤ 0.4 as shown in Fig. 7.b, but at the cost of increased flux swing. Adding the constraints for $li(3)$ only in the last optimization step while keeping the relative cost weight on $li(3)$ low, allows the optimizer to converge to a solution closer to $\psi_{edge} = 0 \forall t$. It is also important to note that the large Ohmic current Fig. 6.j is indicative of a high T_e, high impedance plasma with a large back-EMF and a long resistive timescale (≥ 1000 s). The back-EMF becomes larger as the plasma gets hotter, since plasma resistivity scales with $T_e^{-3/2}$, further increasing the P_{ec} required to overcome it. This is the unfortunate side effect of an inefficient current drive scheme coupled to a heating source. Indeed, the induced current will eventually diffuse away at which point the Ohmic current will go to zero.

Profile evolution, H-mode and transport. The final trajectory state profiles for three time points in the discharge 500 s, 1000s, 1500s are illustrated in Fig. 6.k-o. For the entire duration of the ramp-up we assume that we are in H-mode, since the pedestal is active from the start and is most visible in Fig. 6.o. The q-profile evolution within the constraint is illustrated in Fig. 6.k. Since the q-profile is free to evolve within the constraint, minor current holes develop due to the locations of the ECHCD, but because these are localized it is anticipated they will not cause major instability. If they do become a problem then further optimization will be needed to remove them. The profile eventually settles very close to the desired steady-state, monotonic q-profile. Including a fixed reference q-profile tracker in the cost function was attempted, however this approach consistently resulted in unsatisfactory minimum costs on ψ_{edge}. This indicates that if an ideal time-varying q-profile reference trajectory is not known, then this parameter should be allowed to evolve independently from the cost functions to maximize the reduction of ψ_{edge} and improve convergence. The sharp change in q_{min} in Fig. 6.k at 600 s is due to the sudden spatial movement of q_{min} at $\rho = 0.05$ to $\rho = 0.5$. The sudden movement occurs because there is larger local current being generated at $\rho = 0.5$ and lesser current generated at $\rho = 0.05$, which simultaneously lowers and raises the q profile at these locations respectively.

Sensitivity to the Greenwald fraction. Knowing what initial reference f_{GW} trajectory to execute the ramp with is as much of an initial guess as the initial ECHCD profile. We have guessed that the best route would be at low f_{GW} due to high current drive efficiency at low density. However, the optimization process does not directly show this given any f_{GW} trajectory because the gradient descent will pick either high or low f_{GW} depending on the starting conditions. A loosely defined precipice for this decision seems to be that for $f_{GW} \gtrsim 0.5$ the optimizer will tend toward dominant bootstrap current drive in the high f_{GW} region and for $f_{GW} \leq 0.5$, the optimizer will choose dominant ECHCD in the low f_{GW} region. However, in our simulations we have not managed to converge to suitable $\Delta\psi_{edge}$ in the high f_{GW} region. Operating in the low f_{GW} region has a major impact on the ability for

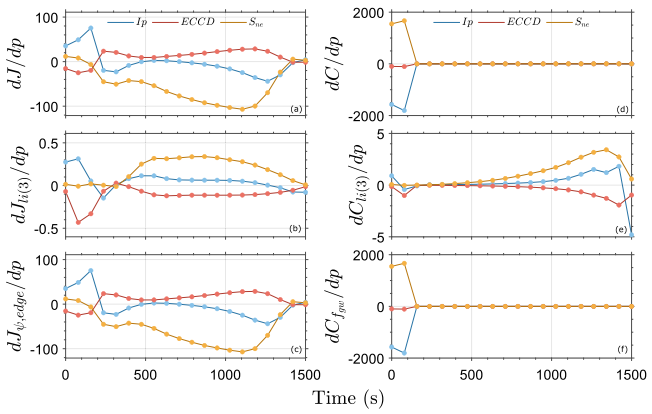

Fig. 7. We can gain insight into the total cost and constraint gradient descent direction for the discharge by plotting of $dJ/dp\&dC/dp$, where the cost and constraint gradients are w.r.t the parametrized control vector described in Section 4.1. The underlying components of cost in this case are $\partial J_{\psi,edge}/\partial p\&\partial J_{li3}/\partial p$. Note that $\partial J_{li3}/\partial p$, is just a fraction of the total cost. Each dot represents a time knot of the control vector which is linked together piece-wise linearly. The constraints shown in (e) and (f) are the upper constraints for f_{GW}, Eq. (33) and $li(3)$,Eq. (37) respectively. Note that before 100 s the upper f_{GW} limit is being exceeded, in (f) we see that the violation is dominantly in the direction of increasing S_{ne} and decreasing I_p.

the plasma to produce alpha power and significant bootstrap fraction. Getting the plasma from this region to a high f_{GW} region with suitable $\Delta\psi_{edge}$, within the constraints is one of the critical challenges in future work.

6. Conclusions

The RAPTOR code has demonstrated its ramp-up scenario development capability on STEP by successfully optimizing the existing ramp-up scenario within desired constraints. This method is unique to STEP ramp-up studies because it provides an alternative to existing trajectory search strategies using JINTRAC, which rely on manually adjusting actuator trajectories to reach a desired state.

Local minima. The highly non-linear and coupled transport model results in a parameter space densely populated with local minima. Objective functions are highly sensitive to initial trajectories and simulations often end in poorly satisfied objective functions or in-feasibility if initial conditions are not chosen carefully. We have demonstrated a method in which these two side effects can be mitigated by gradually building up the objective function and optimizing at each step.

Toward real-time control. The techniques and objective functions developed here are directly applicable to real-time model predictive control, however there is the practical issue of computing solutions to this full RAPTOR model within the millisecond time frame which still needs to be addressed.

7. Future work

Work is currently in progress to identify a trajectory to a steady-state burning plasma with a fusion $Q = \frac{P_{fus}}{P_{heat}} = 11$. More advanced search algorithms will also be explored such as pattern search. Development of dynamic constraints is underway to deal with divertor loading and run-away electrons.

7.1. Extension to stochastic trajectory optimization

The modeling presented utilizes deterministic process models and assumes full knowledge of the current state of the plasma. This is sufficient to generate approximate estimates for current drive actuator heating power and bandwidth. It is however, insufficient to determine how closely the identified trajectory can actually be followed by STEP. To assess the control system trajectory following performance the uncertainties in the process model, partially observed state and actuation need to be considered.

Declaration of competing interest

The authors declare that they have no known competing financial interests or personal relationships that could have appeared to influence the work reported in this paper.

Data availability

Data will be made available on request.

Acknowledgments

The authors would like to thank Federico Felici for his guidance, the RAPTOR development team for useful discussions, Simon Freethy, Ridhima Sharma, Lorenzo Figini, Clive Challis and the STEP team for their advice and support on this work. Thank you to [25] for use of their plotting tools. This research has been funded by STEP, a UKAEA program to design and build a prototype fusion energy plant and a path to commercial fusion.

References

[1] STEP - Spherical Tokamak for Energy Production. URL https://step.ukaea.uk/.

[2] I.A.E. Agency., G. Pereverzev, Plasma Physics and Controlled Nuclear Fusion Research, 1988 : Proceedings of the Twelfth International Conference on Plasma Physics and Controlled Nuclear Fusion Research, Vol. 1, International Atomic Energy Agency, 1989, pp. 739–746, URL https://inis.iaea.org/search/search.aspx?orig_q=RN:20077867.

[3] T. Onchi, H. Idei, M. Fukuyama, D. Ogata, R. Ashida, T. Kariya, A. Ejiri, K. Matsuzaki, Y. Osawa, Y. Peng, S. Kojima, O. Watanabe, M. Hasegawa, K. Nakamura, K. Kuroda, R. Ikezoe, T. Ido, K. Hanada, N. Bertelli, M. Ono, A. Fukuyama, Non-inductive plasma current ramp-up through oblique injection of harmonic electron cyclotron waves on the QUEST spherical tokamak, Phys. Plasmas 28 (2021) http://dx.doi.org/10.1063/5.0031357.

[4] N. Tsujii, Y. Takase, A. Ejiri, T. Shinya, S. Yajima, H. Yamazaki, H. Togashi, C.P. Moeller, B. Roidl, W. Takahashi, K. Toida, Y. Yoshida, Fully non-inductive plasma start-up with lower-hybrid waves using the outboard-launch and top-launch antennas on the TST-2 spherical tokamak, 157, EDP Sciences, 2017, http://dx.doi.org/10.1051/epjconf/201715702009,

[5] R. Raman, D. Mueller, S.C. Jardin, T.R. Jarboe, B.A. Nelson, M.G. Bell, S.P. Gerhardt, E.B. Hooper, S.M. Kaye, C.E. Kessel, J.E. Menard, M. Ono, V. Soukhanovskii, Non-inductive plasma start-up on NSTX and projections to NSTX-U using transient CHI, Nucl. Fusion 53 (2013) http://dx.doi.org/10.1088/0029-5515/53/7/073017.

[6] F.M. Poli, R.G. Andre, N. Bertelli, S.P. Gerhardt, D. Mueller, G. Taylor, Simulations towards the achievement of non-inductive current ramp-up and sustainment in the National Spherical Torus Experiment Upgrade, Nucl. Fusion 55 (2015) http://dx.doi.org/10.1088/0029-5515/55/12/123011.

[7] F. Eriksson, F.J. Casson, C.D. Challis, Y. Baranov, S. Bakes, L. Figini, S. Freethy, T.C. Hender, S. Henderson, H. Kim, K. Kirov, F. Koechl, H. Meyer, R. Sharma, E. Tholerus, C.M. Roach, T.W. CCFE, Current Ramp-Up Modelling for STEP, EPS, 2022, EPS2004 paper (fusenet.eu).

[8] F. Felici, O. Sauter, Non-linear model-based optimization of actuator trajectories for tokamak plasma profile control, Plasma Phys. Control. Fusion 54 (2012) http://dx.doi.org/10.1088/0741-3335/54/2/025002.

[9] A.A. Teplukhina, O. Sauter, F. Felici, A. Merle, D. Kim, Simulation of profile evolution from ramp-up to ramp-down and optimization of tokamak plasma termination with the RAPTOR code, Plasma Phys. Control. Fusion 59 (2017) http://dx.doi.org/10.1088/1361-6587/aa857e.

[10] H. Ltitjens, A. Bondeson, O. Sauter, The CHEASE code for toroidal MHD equilibria, Comput. Phys. Comm. 97 (1996) 219–260.
[11] F. Felici, J. Citrin, A. Teplukhina, J. Redondo, C. Bourdelle, F. Imbeaux, O. Sauter, Real-time-capable prediction of temperature and density profiles in a tokamak using RAPTOR and a first-principle-based transport model, Nucl. Fusion 58 (2018) 096006, http://dx.doi.org/10.1088/1741-4326/aac8f0, URL https://iopscience.iop.org/article/10.1088/1741-4326/aac8f0.
[12] O. Sauter, C. Angioni, Y.R. Lin-Liu, Neoclassical conductivity and bootstrap current formulas for general axisymmetric equilibria and arbitrary collisionality regime, Phys. Plasmas 6 (1999) 2834–2839, http://dx.doi.org/10.1063/1.873240.
[13] F.L. Hinton, R.D. Hazeltine, Theory of plasma transport in toroidal confinement systems, Rev. Modern Phys. 48 (1976) 239–308, http://dx.doi.org/10.1103/RevModPhys.48.239, URL https://link.aps.org/doi/10.1103/RevModPhys.48.239.
[14] D. Farina, A quasi-optical beam-tracing code for electron cyclotron absorption and current drive: GRAY, 52, American Nuclear Society, 2007, pp. 154–160, http://dx.doi.org/10.13182/FST07-A1494,
[15] S.J. Freethy, L. Figini, M. Henderson, 21st Joint Workshop on ECE and ECRH, Cadarache, Cadarache, 2022.
[16] R. Prater, Heating and current drive by electron cyclotron waves, 11, 2004, pp. 2349–2376, http://dx.doi.org/10.1063/1.1690762,
[17] A. Kallenbach, M. Bernert, R. Dux, L. Casali, T. Eich, L. Giannone, A. Herrmann, R. McDermott, A. Mlynek, H.W. Müller, F. Reimold, J. Schweinzer, M. Sertoli, G. Tardini, W. Treutterer, E. Viezzer, R. Wenninger, M. Wischmeier, Impurity seeding for tokamak power exhaust: From present devices via ITER to DEMO, Plasma Phys. Control. Fusion 55 (2013) http://dx.doi.org/10.1088/0741-3335/55/12/124041.
[18] A. Kallenbach, M. Bernert, T. Eich, J.C. Fuchs, L. Giannone, A. Herrmann, J. Schweinzer, W. Treutterer, Optimized tokamak power exhaust with double radiative feedback in ASDEX Upgrade, Nucl. Fusion 52 (2012) http://dx.doi.org/10.1088/0029-5515/52/12/122003.
[19] R. Ochoukov, V. Bobkov, C. Angioni, M. Bernert, M. Dunne, R. Dux, R. Neu, J.M. Noterdaeme, T. Odstrcil, T. Pütterich, F. Reimold, Evolution of ELMY H-mode performance in presence of core radiation on ASDEX Upgrade, in: 42nd European Physical Society Conference on Plasma Physics, EPS 2015, 2015.
[20] P. Rodriguez-Fernandez, N.T. Howard, M.J. Greenwald, A.J. Creely, J.W. Hughes, J.C. Wright, C. Holland, Y. Lin, F. Sciortino, Predictions of core plasma performance for the SPARC tokamak, J. Plasma Phys. (2020) http://dx.doi.org/10.1017/S0022377820001075.
[21] M. Erba, T. Aniel, V. Basiuk, A. Becoulet, X. Litaudon, Validation of a new mixed Bohm/gyro-Bohm model for electron and ion heat transport against the ITER, Tore Supra and START database discharges, Nucl. Fusion 38 (1998) 1013–1028, http://dx.doi.org/10.1088/0029-5515/38/7/305, URL https://iopscience.iop.org/article/10.1088/0029-5515/38/7/305.
[22] F. Wang, Z. Zhao, Z. Wang, Al, F.M. Bhatti, J.W. Essam, Chapter 2: Plasma confinement and transport ITER Physics Expert Groups on Confinement and Transport and Confinement Modelling and Database.
[23] S.M. Kaye, J.W. Connor, C.M. Roach, Thermal confinement and transport in spherical tokamaks: A review, Plasma Phys. Control. Fusion 63 (2021) 123001, http://dx.doi.org/10.1088/1361-6587/ac2b38, URL https://iopscience.iop.org/article/10.1088/1361-6587/ac2b38.
[24] P. Gill, W. Murray, M.H. Wright, Practical Optimization, Springer US, Boston, MA, 2007, http://dx.doi.org/10.1007/978-0-387-71107-2.
[25] A. Aalok, Professional plots, in: MATLAB Central File Exchange, 2022, URL https://www.mathworks.com/matlabcentral/fileexchange/100766-professional-plots.